

# Switching ferromagnetic spins by an ultrafast laser pulse: Emergence of giant optical spin-orbit torque

G. P. ZHANG<sup>1</sup>, Y. H. BAI<sup>2</sup> and THOMAS F. GEORGE<sup>3</sup>

<sup>1</sup> Department of Physics, Indiana State University, Terre Haute, IN 47809, USA

<sup>2</sup> Office of Information Technology, Indiana State University, Terre Haute, IN 47809, USA

<sup>3</sup> Office of the Chancellor and Center for Nanoscience

Departments of Chemistry & Biochemistry and Physics & Astronomy

University of Missouri-St. Louis, St. Louis, MO 63121, USA

PACS 75.78.Jp – Ultrafast magnetization dynamics and switching

PACS 75.40.Gb – Dynamic properties (dynamic susceptibility, spin waves, spin diffusion, dynamic scaling, etc.)

PACS 78.20.Ls – Magneto-optical effects

**Abstract** –Faster magnetic recording technology is indispensable to massive data storage and big data sciences. All-optical spin switching offers a possible solution, but at present it is limited to a handful of expensive and complex rare-earth ferrimagnets. The spin switching in more abundant ferromagnets may significantly expand the scope of all-optical spin switching. Here by studying 40,000 ferromagnetic spins, we show that it is the optical spin-orbit torque that determines the course of spin switching in both ferromagnets and ferrimagnets. Spin switching occurs only if the effective spin angular momentum of each constituent in an alloy exceeds a critical value. Because of the strong exchange coupling, the spin switches much faster in ferromagnets than weakly-coupled ferrimagnets. This establishes a paradigm for all-optical spin switching. The resultant magnetic field (65 T) is so big that it will significantly reduce high current in spintronics, thus representing the beginning of photospintronics.

**Introduction.** – Magnetic switching is the single most important operation for any modern magnetic storage device, where a magnetic field is employed to switch microscopic spins from one direction to another. However, as the areal density increases, the switching speed becomes a major bottleneck for future technological advancement. A possible solution emerged when Beaurepaire *et al.* [1] reported that a 60-fs laser pulse reduced the spin moment of ferromagnetic nickel films within 1 ps. Their finding heralded the arrival of femtomagnetism [2–4], and research efforts intensified immediately [5, 6]. However, for over a decade, the focus has been on demagnetization, not magnetic switching. A major breakthrough came when Stanciu and coworkers [7] demonstrated that a single laser pulse could permanently switch the magnetic spin orientation in amorphous GdFeCo samples. This all-optical helicity-dependent spin switching (AOS) ignited the research community since it may be an alternative to the current magnetic storage technology [4]. However, most AOS samples are amorphous [8,9] and are hard to simulate

without significant approximations. To this end, a unified understanding is still missing, but several promising mechanisms have been proposed, which include the inverse Faraday effect [7,10], spin-flip stimulated Raman scattering [11,12], magnetic circular dichroism [13], magnetic sublattice competition [14], pure thermal effect [15,16] and ultrafast exchange scattering [17]. Recently, Lambert *et al.* [18] reported AOS in an ultrathin ferromagnetic [Co(0.4 nm)/Pt(0.7 nm)]<sub>3</sub> multilayer. Medapalli *et al.* [19] demonstrated that the helicity-dependent switching in Co/Pt proceeds in two steps [20]. Such a system is much more amenable to the simulation without any major approximation, and its magnetic properties have been well known for some time [21]. It is likely that a detailed study of such a system may shed new light on AOS.

**Spin reversal theory.** – We employ a thin film of  $101 \times 101 \times 4$  or 40,804 lattice sites in a simple cubic structure (see the top half of Fig. 1) with an open boundary condition. Each site has a spin  $\mathbf{S}_i$  which is exchange-coupled to the nearest neighboring spins through the ex-

change interaction  $J_{ex}$ . Our Hamiltonian [22–25], which is often used in magnetic multilayers [26], is

$$H = \sum_i \left[ \frac{\mathbf{p}_i^2}{2m} + V(\mathbf{r}_i) + \lambda \mathbf{L}_i \cdot \mathbf{S}_i - e \mathbf{E}(\mathbf{r}, t) \cdot \mathbf{r}_i \right] - \sum_{ij} J_{ex} \mathbf{S}_i \cdot \mathbf{S}_j, \quad (1)$$

where the first term is the kinetic energy operator of the electron, the second term is the potential energy operator,  $\lambda$  is the spin-orbit coupling in units of  $\text{eV}/\hbar^2$ ,  $\mathbf{L}_i$  and  $\mathbf{S}_i$  are the orbital and spin angular momenta at site  $i$  in the unit of  $\hbar$ , respectively, and  $\mathbf{p}$  and  $\mathbf{r}$  are the momentum and position operators of the electron, respectively. To minimize the number of parameters, we choose a spherical harmonic potential  $V(\mathbf{r}_i) = \frac{1}{2} m \Omega^2 \mathbf{r}_i^2$  with system frequency  $\Omega$ , but this approximation can be lifted when accurate potentials are known. Our model represents a small step towards a complete model. We assume that the electron moves along the  $z$  axis with an initial velocity of 1 nm/fs in the harmonic potential, so the initial orbital angular momentum is zero. The last term is the exchange interaction, and  $J_{ex}$  is the exchange integral in units of  $\text{eV}/\hbar^2$ . Although our main interest is in ferromagnets, the same Hamiltonian can describe both antiferromagnets and ferrimagnets. Such a Hamiltonian contains the necessary ingredients for AOS.

Figure 1 shows that a laser pulse propagates along the  $+z$  axis; its amplitude is attenuated according to Beer's law  $e^{-z/d}$  (along  $+z$ ), where  $d$  is the penetration depth. The bottom half of Fig. 1 illustrates our idea of spin torque to switch spins. For convenience, the spatial dimension is measured in the unit of the lattice site number along each direction, so that all the spatial variables are dimensionless or in the unit of the site number. The laser spot is centered at  $x_c = 51$  and  $y_c = 51$  with radius  $r$  and lateral spatial profile [10]  $e^{-[(x-x_c)^2 + (y-y_c)^2]/r^2}$  (in the  $xy$  plane). The laser electric field is described by

$$\mathbf{E}(\mathbf{r}, t) = \mathbf{A}(t) \exp\left[-\frac{(x-x_c)^2 + (y-y_c)^2}{r^2} - \frac{z}{d}\right], \quad (2)$$

where  $x$  and  $y$  are the coordinates in the unit of the site number. Since in the following our spins are all initialized along the  $-z$  axis, we choose a left-circularly polarized field  $\mathbf{A}(t)$  which has a Gaussian shape  $\mathbf{A}(t) = A_0 e^{-t^2/T^2} [-\sin(\omega t) \hat{x} + \cos(\omega t) \hat{y}]$ , where  $\omega$  is the laser carrier frequency,  $T$  is the laser pulse duration,  $A_0$  is the laser field amplitude,  $t$  is time,  $\hat{x}$  and  $\hat{y}$  are unit vectors, respectively. We choose  $T = 100$  fs. We only consider a resonant excitation where the laser photon energy  $\hbar\omega = 1.6$  eV matches the system energy  $\hbar\Omega$ ; for an off-resonant excitation, we refer the reader to a prior study [24]. In transition metals, the penetration depth is about 14 nm, which corresponds to 30 layers, so we choose  $d = 30$ . To compute the spin evolution, we employ the Heisenberg's equation of motion,  $i\hbar\dot{\mathbf{A}} = [\mathbf{A}, H]$ , where we make the

time-dependent Hartree-Fock approximation, so that all the operators are replaced by their respective expectation values, and then we solve the equation numerically. Our calculation of the spin change is similar to that of Wienholdt *et al.* [27] though they used a thermal field.

**Dependence of spin switching on spin angular momentum.** — We choose eight initial spin momenta  $S_z(0)$  from  $0.2\hbar$  to  $1.6\hbar$  in steps of  $0.2\hbar$ , which covers most magnetic materials. For each  $S_z(0)$ , we vary the laser field amplitude [3, 19]  $A_0$  from 0.01 to 0.08 V/Å in steps of 0.002 V/Å. This step is tedious but necessary, since different  $S_z(0)$  have different optimal field amplitudes for spin reversal. We fix the spin-orbit coupling at  $\lambda = 0.06 \text{ eV}/\hbar^2$ , the exchange interaction  $J_{ex}$  at  $1 \text{ eV}/\hbar^2$ , and the spot radius of  $r = 100$ . The spins are initialized along the  $-z$  axis, equivalent to applying a magnetic uniaxial anisotropy. A spin reversal is considered achieved if the  $z$  component spin angular momentum  $S_z$  changes from a negative value to a large and positive value at the end of the dynamics. Figure 2(a) shows the normalized and system-averaged spin as a function of time for each  $S_z(0)$  at its respective optimal laser field amplitude. All the curves, except  $S_z(0) = 0.2\hbar$ , are vertically shifted for clarity. The dotted horizontal lines denote  $0\hbar$ . We start with  $S_z(0) = 0.2\hbar$ , and we see that the spin does not switch and only oscillates around  $0\hbar$  with a period determined by the product of  $\lambda$  and  $S_z(0)$  [24, 28]. When we increase  $S_z(0)$  to  $0.4\hbar$ , the oscillation is attenuated and the final spin is barely above  $0\hbar$ . And the situation does not change much for  $S_z(0) = 0.6\hbar$ . However, when we continue to increase  $S_z(0)$  above  $0.8\hbar$ , the spin ringing is strongly reduced, and the final spin settles down at a large positive value, an indication of spin reversal. Above  $0.8\hbar$ , the situation gets better. For this reason, we define a critical spin angular momentum  $S_z^c = 0.8 \pm 0.2\hbar$  for AOS.

To quantify AOS, we define the spin switchability as  $\eta = \frac{S_z^f}{S_z(0)} \times 100\%$ , where  $S_z^f$  is the final spin angular momentum. This definition is different from that of Vahaplar *et al.* [10]. We fix  $S_z(0) = 1.2\hbar$ , but change the spin-orbit coupling  $\lambda$ . Note that our conclusions are the same for different  $S_z(0)$  as far as it is above  $S_z^c$ . Figure 2(b) shows that a minimum  $\lambda$  of  $0.04 \text{ eV}/\hbar^2$  is required to reverse spins. Too small a  $\lambda$  only leads to a strong spin oscillation, regardless of the laser field amplitude. This indicates a unique role of spin-orbit coupling (SOC) in AOS. The roles of the exchange interaction and laser field amplitude are shown in Fig. 2(c), where we fix  $S_z(0) = 1.2\hbar$ ,  $r = 100$  and  $\lambda = 0.06 \text{ eV}/\hbar^2$ . We notice that as  $A_0$  increases,  $S_z$  sharply increases and reaches its maximum. If we increase it further,  $S_z$  is reduced since the spin overshoots, and an asymmetric peak is formed. This constitutes our first criterion that the laser amplitude must fall into a narrow region for AOS to occur. This is consistent with Medapalli *et al.*'s finding (see Fig. 1(c) of their paper [19]); such a helicity-dependent switching also agrees with another study by El Hadri *et al.* [20]. These agreements do

not necessarily validate all the aspects of our model but instead they simply suggest that our model may offer an alternative to the existing models. If we increase  $A_0$  further, a second peak appears since the spin re-switching starts. These double peaks do not appear for a smaller  $S_z(0)$ . We find that the exchange does not change this dependence a lot.

**Phase diagram of spin reversal.** – We construct a phase diagram of spin reversal ( $\eta - S_z(0)$ ) in Fig. 3(a) for thirteen  $S_z(0)$ 's and two radii of the laser spot,  $r = 100$  and 50. For  $\eta$  to exceed 50-60%,  $S_z(0)$  must be higher than the critical value of  $S_z^c = 0.8 \pm 0.2\hbar$ . The long-dashed line denotes  $S_z^c$ . We see that the nickel's spin momentum is well below  $S_z^c$ , which explains why nickel has never been used for AOS. Co is on the threshold. In Co-Pt granular samples [29], the effective spin magnetic moment per  $3d$  hole is  $0.77 \mu_B$ ; since there are 2.49-2.62 holes, the spin angular momentum is  $0.96\hbar$ , satisfying this criterion. In the ultrathin ferromagnetic  $[\text{Co}(0.4 \text{ nm})/\text{Pt}(0.7 \text{ nm})]_3$  films [18], due to the reduced dimensionality, the enhanced spin moment greatly increases the chance for AOS. The empty boxes in Fig. 3(a) represent the case with  $r = 50$  (which is close to the switch limit), where only a small portion of the sample is exposed to the laser light. We see that the switchability reduces sharply since the laser fluence on lattice sites away from the center of the laser beam becomes very weak and is not strong enough to reverse spins on those sites. Since the essence of AOS is rooted in spin-orbit coupling and all the switchabilities are obtained at the optimal field amplitude, we do not expect that a more accurate potential would change the phase diagram strongly. Our criterion not only applies to ferromagnets, but also to ferrimagnets. Figure 3(b) illustrates that each of the major elements in all the 11 GdFeCo and TbFe alloys [30] has the effective spin above  $S_z^c$ . This constitutes strong evidence that our finding has a broader impact on the ongoing research in all-optical spin switching.

**Emergence of optical spin-orbit torque.** – While the effect of the laser field amplitude on AOS is obvious [31], how the initial spin  $S_z(0)$  affects the spin switching is not obvious. We examine how the spin evolves with time. For a spin at site  $i$ , the spin angular momentum  $\mathbf{S}$  precedes according to

$$\frac{d\mathbf{S}_i}{dt} = \sum_{j(i)} J_{ex} \mathbf{S}_i \times \mathbf{S}_j + \lambda(\mathbf{L}_i \times \mathbf{S}_i), \quad (3)$$

where the two driving terms on the right-hand side represent two torques. The first is the Heisenberg exchange torque  $\tau_{ex} = \sum_{j(i)} J_{ex} \mathbf{S}_i \times \mathbf{S}_j$ . Since all the spins are ferromagnetically ordered, this torque is very small. The second one is the spin-orbit torque (SOT),  $\tau_{soc} = \lambda(\mathbf{L}_i \times \mathbf{S}_i)$ , which may serve as a source term for the inverse Faraday effect [32, 33]. Before the laser excitation,  $\tau_{soc}$  is small, since in solids the orbital angular momentum  $\mathbf{L}$  is largely quenched. With the arrival of the laser pulse,  $\mathbf{L}$  is boosted

sharply [32] (see Fig. 4) and helicity-dependent, where  $J_{ex} = 1\text{eV}/\hbar^2$ , and  $S_z(0) = 1.2\hbar$ , but three components of the orbital angular momentum behave differently.  $L_x$  and  $L_y$  are mostly negative, but  $L_z$  is positive. Around 50 fs,  $L_x$  reaches  $-0.24\hbar$ , while  $L_y$  swings to  $-0.16\hbar$  and the change in  $L_z$  is smaller, around  $0.04\hbar$ . All three components settle down to zero around 200 fs. This is very important, since if the orbital momentum were big after the laser field is gone, the spin would oscillate very strongly and could not be reversed faithfully. Thus, through the spin-orbit coupling, the laser field increases the orbital angular momentum, and subsequently  $\tau_{soc}$  is boosted. For this reason, Tesavova *et al.* [34] called  $\tau_{soc}$  the optical spin-orbit torque, or femtosecond spin-orbit torque by Lingos *et al.* [35].

We choose two initial spin momenta,  $S_z(0) = 0.3\hbar$  and  $1.2\hbar$ , with all the spins initialized along the  $-z$  axis (see the light blue arrows in Figs. 5(a) and (b)). Figure 5(a) shows that at  $0.3\hbar$  the spin undergoes strong oscillations and shows many spirals, but does not settle down to the  $+z$  axis after the laser pulse is gone (see the red arrow). By contrast, at  $1.2\hbar$  the spin flips over from the  $-z$  to  $+z$  axis within 110 fs, without strong oscillation (see the solid red arrow). To understand why the initial spin angular momentum has such a strong effect on AOS, Figure 5(c) shows that  $\tau_{soc}$  at  $0.3\hbar$  is very weak, around  $0.01 \hbar/\text{fs}$ , and more importantly, it rapidly swings between positive and negative values, both of which are detrimental to the spin reversal. At  $S_z(0) = 1.2\hbar$ ,  $\tau_{soc}$  is positive and large, which allows the spin to switch over successfully. This suggests that SOT offers an alternative path to AOS (see the bottom figure of Fig. 1), and it acts like an effective magnetic field, which has been sought after in the literature [10, 15] for nearly a decade. At  $1.2\hbar$ , we time-integrate the torque from -200 to +200 fs and find that the time-averaged torque corresponds to 65 T of a magnetic field. In spintronics, the spin transfer torque heavily relies on the high electric current [26, 36]. Such a large SOT, if implemented in real experiments, should significantly reduce the requirement of huge electric current for spintronics [37], and thus opens a door for rapid applications in storage technology [38].

**Conclusion.** – We have investigated all-optical spin switching in 40,000 ferromagnetic spins. We identify that it is the laser-induced optical spin-orbit torque that determines the fate of spin switching. The spin-orbit torque sensitively depends on the value of the initial spin momentum of each active element in a sample, regardless of the types of magnets. To switch, each active element must have its effective spin angular momentum larger than  $(0.8 \pm 0.2)\hbar$ . This means that the switchability in Fe, Gd and Tb is likely to be higher than Co and Ni. PMA observed in various AOS materials [9] seems to be an indication of enhanced spin moment, which is in line with our theory. The ps all-optical spin switching observed in ferrimagnets is associated with the weak exchange coupling;

in ferromagnets, with a stronger coupling, the switching is much faster. SOT is so large that it will significantly reduce the electric current used in spintronics. After our present study was finished, we noticed a recent publication by Bokor's group [37] to use a laser to assist magnetization reversal. A combination of photonics and spintronics represents the arrival of photospintronics [39].

\* \* \*

We would like to thank Dr. Hassdenteufel for sending us the experimental results [30]. This work was solely supported by the U.S. Department of Energy under Contract No. DE-FG02-06ER46304. Part of the work was done on Indiana State University's quantum cluster and high-performance computers. The research used resources of the National Energy Research Scientific Computing Center, which is supported by the Office of Science of the U.S. Department of Energy under Contract No. DE-AC02-05CH11231. This work was performed, in part, at the Center for Integrated Nanotechnologies, an Office of Science User Facility operated for the U.S. Department of Energy (DOE) Office of Science by Los Alamos National Laboratory (Contract DE-AC52-06NA25396) and Sandia National Laboratories (Contract DE-AC04-94AL85000).

## REFERENCES

- [1] E. Beaupaire, J. C. Merle, A. Daunois, and J.-Y. Bigot, *Phys. Rev. Lett.* **76**, 4250 (1996).
- [2] G. P. Zhang, W. Hübner, E. Beaupaire, and J.-Y. Bigot, *Topics Appl. Phys.* **83**, 245 (2002).
- [3] G. P. Zhang and W. Hübner, *Phys. Rev. Lett.* **85**, 3025 (2000).
- [4] A. Kirilyuk, A. V. Kimel, and Th. Rasing, *Rev. Mod. Phys.* **82**, 2731 (2010).
- [5] A. V. Kimel, A. Kirilyuk, P. A. Usachev, R. V. Pisarev, A. M. Balbashov, and Th. Rasing, *Nature* **435**, 655 (2005).
- [6] G. P. Zhang, W. Hübner, G. Lefkidis, Y. Bai, and T. F. George, *Nature Phys.* **5**, 499 (2009).
- [7] C. D. Stanciu, F. Hansteen, A. V. Kimel, A. Kirilyuk, A. Tsukamoto, A. Itoh, and Th. Rasing, *Phys. Rev. Lett.* **99**, 047601 (2007).
- [8] A. Hassdenteufel, B. Hebler, C. Schubert, A. Liebig, M. Teich, M. Helm, M. Aeschlimann, M. Albrecht, and R. Bratschitsch, *Adv. Mater.* **25**, 3122 (2013).
- [9] S. Mangin, M. Gottwald, C.-H. Lambert, D. Steil, V. Uhler, L. Pang, M. Hehn, S. Alebrand, M. Cinchetti, G. Malinowski *et al.*, *Nature Mater.* **13**, 286 (2014).
- [10] K. Vahaplar, A. M. Kalashnikova, A. V. Kimel, S. Gerlach, D. Hinzke, U. Nowak, R. Chantrell, A. Tsukamoto, A. Itoh, A. Kirilyuk *et al.*, *Phys. Rev. B* **85**, 104402 (2012).
- [11] V. N. Gridnev, *Phys. Rev. B* **77**, 094426 (2008).
- [12] D. Popova, A. Bringer, and S. Blügel, *Phys. Rev. B* **85**, 094419 (2012).
- [13] A. R. Khorsand, M. Savoini, A. Kirilyuk, A. V. Kimel, A. Tsukamoto, A. Itoh, and Th. Rasing, *Phys. Rev. Lett.* **108**, 127205 (2012).
- [14] J. H. Mentink, J. Hellsvik, D. V. Afanasiev, B. A. Ivanov, A. Kirilyuk, A. V. Kimel, O. Eriksson, M. I. Katsnelson, and Th. Rasing, *Phys. Rev. Lett.* **108**, 057202 (2012).
- [15] T. A. Ostler, J. Barker, R. F. L. Evans, R. W. Chantrell, U. Atxitia, O. Chubykalo-Fesenko, S. El Moussaoui, L. Le Guyader, E. Mengotti, L.J. Heyderman *et al.*, *Nat. Commun.* **3**, 666 (2012).
- [16] U. Atxitia, T. Ostler, J. Barker, R. F. L. Evans, R. W. Chantrell, and O. Chubykalo-Fesenko, *Phys. Rev. B* **87**, 224417 (2013).
- [17] A. Baral and H. C. Schneider, *Phys. Rev. B* **91**, 100402(R) (2015).
- [18] C.-H. Lambert, S. Mangin, B. S. D. Ch. S. Varaprasad, Y. K. Takahashi, M. Hehn, M. Cinchetti, G. Malinowski, K. Hono, Y. Fainman, M. Aeschlimann *et al.*, *Science* **345**, 1337 (2014).
- [19] R. Medapalli, D. Afanasiev, D. K. Kim, Y. Quessab, S. Manna, S. A. Montoya, A. Kirilyuk, Th. Rasing, A. V. Kimel, and E. E. Fullerton, arXiv: 1607.02502v1 (2016).
- [20] M. S. El Hadri, P. Pirro, C.-H. Lambert, S. Petit-Watelot, Y. Quessab, M. Hehn, F. Montaigne, G. Malinowski, and S. Mangin, *Phys. Rev. B* **94**, 064412 (2016).
- [21] P. Soderlind, O. Eriksson, B. Johansson, R. C. Albers, and A. M. Boring, *Phys. Rev. B* **45**, 12911 (1992).
- [22] G. P. Zhang, *J. Phys.: Condens. Mat.* **23**, 206005 (2011).
- [23] G. P. Zhang and T. F. George, *J. Phys.: Condens. Mat.* **25**, 366002 (2013).
- [24] G. P. Zhang, Y. H. Bai, and T. F. George, *Europhys. Lett.* **112**, 27001 (2015).
- [25] G. P. Zhang, T. Latta, Z. Babyak, Y. H. Bai, and T. F. George, *Modern Physics Letters B* **30**, 1630005 (2016).
- [26] P. M. Haney and M. D. Stiles, *Phys. Rev. Lett.* **105**, 126602 (2010).
- [27] S. Wienholdt *et al.*, *Phys. Rev. B* **88**, 020406 (2013).
- [28] G. P. Zhang, M. S. Si, and T. F. George, *J. Appl. Phys.* **117**, 17D706 (2015).
- [29] A. I. Figueroa, J. Bartolomé, L. M. Garca, F. Bartolom, O. Bunau, J. Stankiewicz, L. Ruiz, J. M. Gonzalez-Calbet, F. Petroff, C. Deranlot *et al.*, *Phys. Rev. B* **90**, 174421 (2014).
- [30] A. Hassdenteufel, J. Schmidt, C. Schubert, B. Hebler, M. Helm, M. Albrecht, and R. Bratschitsch, *Phys. Rev. B* **91**, 104431 (2015).
- [31] K. Vahaplar, A. M. Kalashnikova, A. V. Kimel, D. Hinzke, U. Nowak, R. Chantrell, A. Tsukamoto, A. Itoh, A. Kirilyuk, and Th. Rasing, *Phys. Rev. Lett.* **103**, 117201 (2009).
- [32] R. John *et al.*, arXiv: 1606.08723 (2016).
- [33] M. Berritta *et al.*, arXiv:1604.01188v1 (2016).
- [34] N. Tesarova, P. Nemec, E. Rozkotova, J. Zemen, T. Janda, D. Butkovicova, F. Trojanek, K. Olejnik, V. Novak, P. Maly *et al.*, *Nat. Photonics* **7**, 492 (2013).
- [35] P. C. Lingos, J. Wang, and I. E. Perakis, *Phys. Rev. B* **91**, 195203 (2015).
- [36] D. C. Ralph and M. D. Stiles, *J. Magn. Magn. Mater.* **320**, 1190 (2008).
- [37] J. Bokor (private communication). Here the laser-induced spin-orbit torque was used to reverse magnetization.
- [38] S. A. Wolf, D. D. Awschalom, R. A. Buhrman, J. M. Daughton, S. von Molnar, M. L. Roukes, A. Y. Chtchelkanova, and D. M. Treger, *Science* **294**, 1488 (2001).
- [39] P. C. Mondal, P. Roy, D. Kim, E. E. Fullerton, H. Cohen, and R. Naaman, *Nano Lett.* **16**, 2806 (2016).



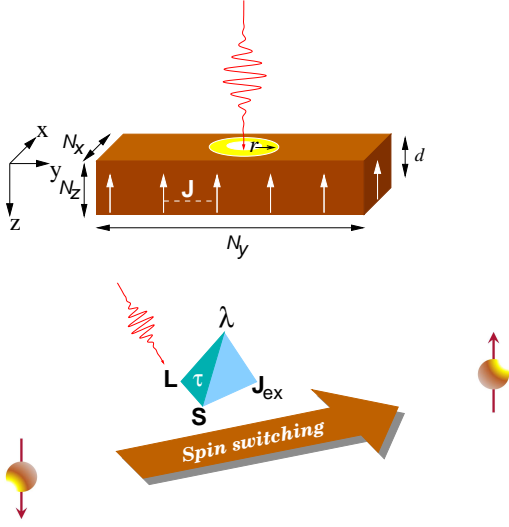


Fig. 1: All-optical spin switching in ferromagnets. (Top) The simulated sample has the dimensions  $(N_x = 101) \times (N_y = 101) \times (N_z = 4)$ , more than 40,000 spins. The light propagates along the  $+z$  direction with penetration depth  $d$  and radius of the spot  $r$ . (Bottom) The laser-induced optical spin-orbit torque provides the necessary torque to reverse the spin.

[40] B. Szpunar and B. Kozarzewski, Phys. Stat. Sol. (b) **82**, 205 (1977).

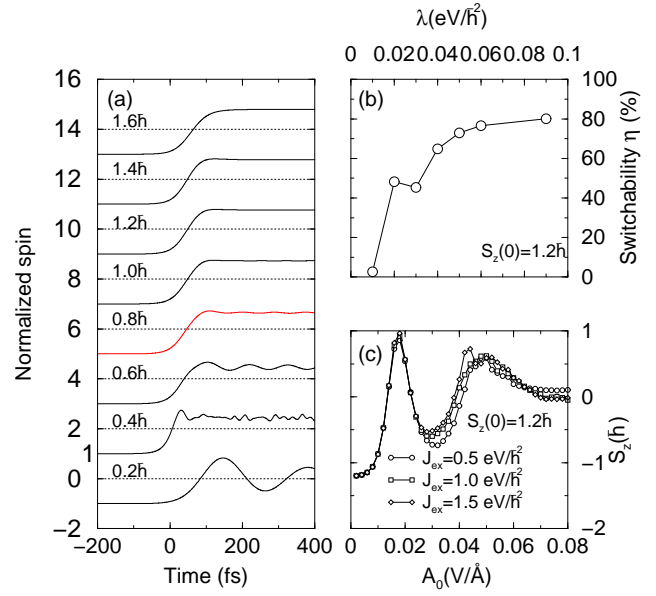


Fig. 2: (a) Time evolution of the  $z$  component of the normalized and system-averaged spin angular momentum for eight initial spin values  $S_z(0)$  from  $0.2\hbar$  to  $1.6\hbar$ . The spin reversal realized starts once  $S_z(0)$  is around and above  $0.8\hbar$ . (b) Switchability as a function of spin-orbit coupling. The critical value is around  $0.04 \text{ eV}/\hbar^2$ . (c) Dependence of the final spin on the laser field amplitude for three values of the exchange integral  $J_{ex}$ .

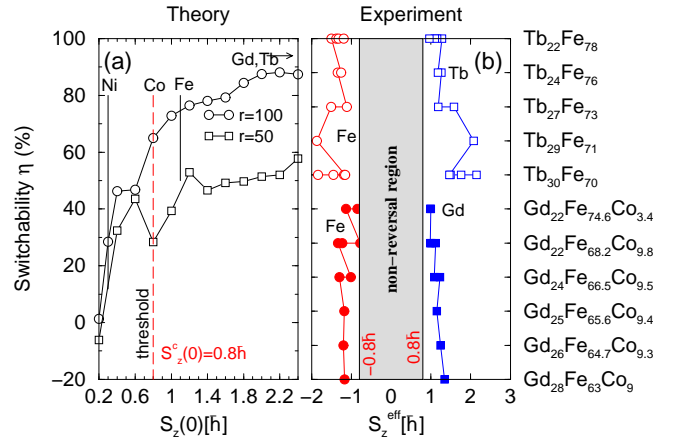


Fig. 3: (a) Phase diagram of the spin switchability versus the initial spin angular momentum  $S_z(0)$  at the respective optimal laser field amplitudes. The empty circles and boxes refer to the results with  $r = 100$  and  $r = 50$ , respectively. The long-dashed line denotes the critical spin  $S_z^c$ . Two thin vertical lines represent the spins for Ni and Fe. Co is on the border line, while Gd and Tb are way above  $S_z^c$ . (b) Computed experimental effective spin angular momentum for each element in 11 GdFeCo and TbFe alloys [30]. Without exception, all elements have spin larger than  $S_z^c$ .

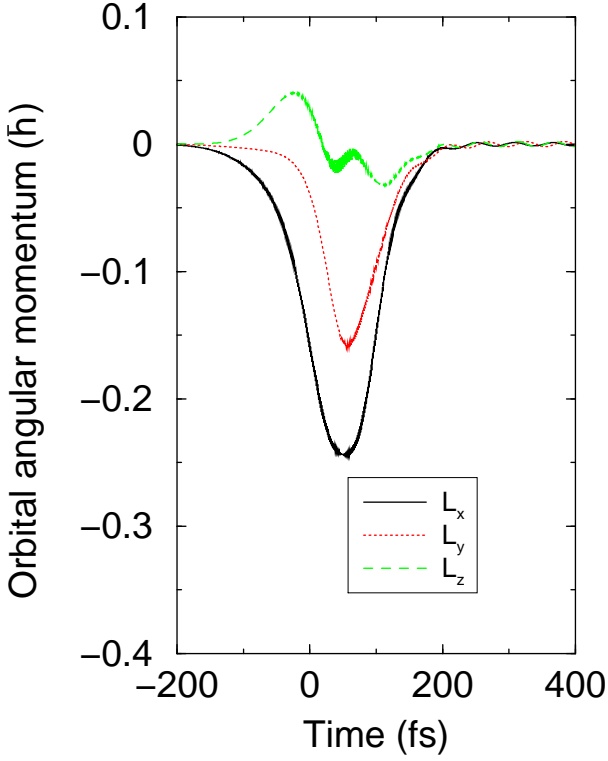


Fig. 4: Orbital angular momentum change as a function of time. Here  $J_{ex} = 1\text{eV}/\hbar^2$ , and  $S_z(0) = 1.2\hbar$ . The laser amplitude is at its optimal value of  $0.018\text{V}/\text{\AA}$ . The solid, dotted and dashed lines denote  $L_x$ ,  $L_y$  and  $L_z$  components [25], respectively.

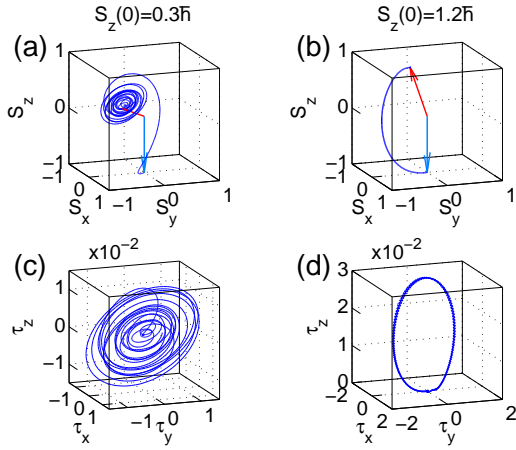


Fig. 5: (a) Precession of the normalized spin angular momentum in 3-dimensional space at  $S_z(0) = 0.3\hbar$ . The blue arrow denotes the initial spin, and the red one the final spin. The trace of the final spin forms a spiral and the spin does not switch. (b) The normalized spin angular momentum at  $S_z(0) = 1.2\hbar$  is directly switched from the  $-z$  to  $+z$  axis without precession [25]. (c) Time evolution of the spin-orbit torque at  $S_z(0) = 0.3\hbar$ . The torque is zero in the beginning. All the torques are in the units of  $\hbar/\text{fs}$ . (d) Same as (c) but for  $S_z(0) = 1.2\hbar$  [25].

### Supplementary Materials

A main difference between ferrimagnets and ferromagnets is that ferrimagnets have magnetic sublattices while ferromagnets do not. To directly apply our results to ferrimagnets, we need to understand whether these magnetic sublattice spins behave similarly to those spins in ferromagnets. Fortunately, we find that according to our simulation, at least in the weak laser field limit, left(right)-circularly polarized light only switches spin from down(up) to up(down), not the other way around. Therefore, flipping a sublattice spin in ferrimagnets is equivalent to flipping a spin in ferromagnets. This is the theoretical basis to apply our theory to ferrimagnets.

In the following, we explain how the spin angular momentum is computed from the experimental data. Experimentally, the measured magnetic property is often the remanent magnetization  $m_R$  in units of  $10^3 \text{ A/m}$ , or equivalently  $\text{emu/cc}$  [30]. To convert magnetization to spin angular momentum, we need the volume of the sample, but experimentally the volume of the sample is not given. This makes a quantitative comparison nearly impossible.

We find a simple and powerful method which does not rely on the experimental volume. Take  $R_x T_{1-x}$  alloy as an example, where R stands for Tb or Gd and T stands for Fe. We ignore Co since its concentration is too low. We first compute the effective volume

$$V_{eff} = xV_R + (1-x)V_T, \quad (4)$$

where  $V_R$  and  $V_T$  are the supercell volume of pure element R and T. Tb has a hcp structure, with the lattice constants  $a = 3.601 \text{ \AA}$  and  $c = 5.6936 \text{ \AA}$ ; Fe has a bcc structure with  $a = 2.8665 \text{ \AA}$ . Then we multiply  $m_R$  by  $V_{eff}$  to get the effective spin moment for the alloy, i.e.,  $M_{eff} = m_R V_{eff}$ . Since  $M_{eff}$  is in the units of  $[\text{Am}^2]$ , we convert it to the Bohr magneton  $\mu_B$ , with the conversion factor of  $0.10783 \times 10^{-3}$ .

Szpunar and Kozarzewski [40] carried out extensive calculations on transition-metal and rare-earth intermetallic compounds by comparing their results with the experimental ones, and concluded that it is reasonable to assume that the average magnetic moments of the transition metals and of the rare earth metals are roughly independent of structures. Then, the effective spin moment  $M_{eff}$  can be approximately written as

$$M_{eff} = xM_R + (1-x)M_T \equiv M_R^{eff} + M_T^{eff}, \quad (5)$$

where  $M_R$  and  $M_T$  are the spin moments of pure R and T, respectively. Here the last equation defines the effective spin moment for R and T.

However, this single equation is not enough to compute  $M_R$  and  $M_T$  since there are two unknowns for a single equation. The trick is that we use two sets of compositions,  $x_1$  and  $x_2$ , so we have two equations,

$$M_{eff}^{(1)} = x_1 M_R + (1-x_1) M_T \quad (6)$$

$$M_{eff}^{(2)} = x_2 M_R + (1-x_2) M_T, \quad (7)$$

where  $M_{eff}^{(1)} = m_R^{(1)} V_{eff}^{(1)}$  and  $M_{eff}^{(2)} = m_R^{(2)} V_{eff}^{(2)}$ . Here again we rely on the assumptions that  $M_R$  and  $M_T$  do not change much with composition change from  $x_1$  to  $x_2$ . When we choose  $x_1$  and  $x_2$ , we are always careful whether  $M_R$  or  $M_T$  changes sign, since experimentally the reported values are the absolute value. In addition, it is always better to choose those  $x_1$  and  $x_2$  which have the same sign of  $M_R$  and  $M_T$ . Choosing several different pairs of  $(x_1, x_2)$  is crucial to a reliable result. Solving the above two equations, we can find  $M_R$  and  $M_T$ .

Before we compute the spin angular momentum, we check whether the computed spin moments  $M_R$  and  $M_T$  (in the units of  $\mu_B$ ) are within the respective value of each pure element, i.e.,  $M_{Gd}^o = 7.63\mu_B$ ,  $M_{Tb}^o = 9.34\mu_B$ , and  $M_{Fe}^o = 2.2\mu_B$ . If the computed spin moment ( $M_R$  and  $M_T$ ) is far off from those spin moments, this indicates that either our method or the experimental result is not reliable; as a result, their spin angular momentum is not included in our figure, but is included here. Once the spin moment passes this test, we proceed to convert the spin moment to spin angular momentum.

Our method works better for Gd alloys than Tb alloys, since the former has zero orbital angular momentum but the latter has a nonzero orbital angular momentum. For Gd and Fe, the orbital momentum is largely quenched. Assuming that the Lande  $g$ -factor is 2, we divide the spin moments  $M_R$  and  $M_T$  by 2 to get the spin angular momentum  $S_R$  and  $S_T$  in the unit of  $\hbar$ . To get the effective spin angular momentum, we multiply  $S_R$  and  $S_T$  with  $x$  and  $1-x$ , respectively, i.e.,

$$S_R^{eff} = xS_R \quad (8)$$

$$S_T^{eff} = (1-x)S_T. \quad (9)$$

It is these two effective spin angular momenta that we apply our above criterion to. For Tb, our results have an uncertainty since its orbital angular momentum in its alloys is unknown, although its orbital angular momentum in pure Tb metal is  $3.03\hbar$ . Table 1 shows the orbital-free spin angular momentum for 11 alloys, where we adopt a simple cubic structure for Fe since it matches the experimental values better. These data are used to plot Fig. 3(b) of the main paper.

Before we show all the details of our results, we wish to present an example how the spin moment changes with the concentration under our assumption. Since R and T are ferrimagnetically coupled and  $M_R$  and  $M_T$  differ by a sign,  $M_{eff}$  changes from a positive value to a negative as the composition  $x$  changes. Figure 6 shows such an example, where we use the experimental value  $M_{Gd} = 7.63\mu_B$  of pure Gd and  $M_{Fe} = 2.2\mu_B$  of pure Fe. A V shape curve is formed, the same as the experiment [30].  $M_{eff}$  is close to zero around  $x = 0.22$ . The effective spin momenta  $S_{Gd}^{eff}$  for Gd and  $S_{Fe}^{eff}$  for Fe are also shown (use the right axis). As  $x$  increases,  $S_{Gd}^{eff}$  increases but  $|S_{Fe}^{eff}|$  is reduced. Two long-dashed lines denote our critical values  $\pm S_z^c$ . We use the dotted line box to bracket the narrow

window for spin switching. Since this window is very close to the compensation point (in term of the concentration  $x$ ), this explains why Hassdenteufel *et al.* [8] found that the low remnant magnetization for AOS must be below 125 emu/cc. This is the direct consequence of the requirement of the critical value of  $S_z^c$ .

In the following, we tabulate all the computed results for both GdFeCo and TbFe alloys, respectively. All the tables start with the spin moment for each element, followed by the effective spin angular momentum for each element in the alloys. To reduce possible errors in those experimental data, we always choose multiple pairs of data for the same alloy.

**Gd alloys.** We start with a pair of Gd<sub>24</sub>Fe<sub>66.5</sub>Co<sub>9.5</sub> and Gd<sub>22</sub>Fe<sub>68.2</sub>Co<sub>9.8</sub>. Table 2 (the first two rows) shows that Gd has a magnetic moment of  $-10.2187\mu_B$  and Fe  $3.9149\mu_B$ , respectively, where we purposely keep more significant figures to show the accuracy of our results. Note that Gd and Fe are ferrimagnetically coupled, so they differ by a negative sign. By comparing them with their respective element values, we conclude that these moments are reasonable. We then compute the effective spin angular momentum for Gd and Fe (see the third and fourth columns). Clearly, both numbers are larger than our critical spin angular momentum. Then we compute four additional combinations of alloys. If the experimental results were exact and free of any error, the obtained effective spin angular momentum should not change. However, in reality, they do change, but we find that the change for Gd alloys is very small. For instance, Gd<sub>22</sub>Fe<sub>68.2</sub>Co<sub>9.8</sub> is used twice, but each case has a similar  $S_{Gd}^{eff}$  and  $S_{Fe}^{eff}$  (compare the first pair and third pair). The same is also true for Gd<sub>22</sub>Fe<sub>74.6</sub>Co<sub>3.4</sub>, but when we pair Gd<sub>22</sub>Fe<sub>68.2</sub>Co<sub>9.8</sub> with Gd<sub>22</sub>Fe<sub>74.6</sub>Co<sub>3.4</sub>, we find a slightly larger change. The reason is easy to understand since these two compounds have a very similar composition, and the relative error becomes larger.

Table 3 assumes a bcc structure for Fe. Here the values are all reduced somewhat, but the main conclusion remains the same. We also find that the biggest error comes from the alloy pairs with a similar composition (see the last pair). We notice that  $S_{Fe}^{eff}$  is slightly below our critical value. It is likely that the larger relative error when two compositions are close is responsible for the discrepancy.

**Tb alloys.** In comparison with Gd alloys, Tb alloys are more prone to errors, since their orbital momentum is not completely quenched. Table 4 shows two different stories. For the first seven pairs, we see that all the moments for Tb and Fe are reasonably close to their respective element moments. But for the last two pairs, their values are way too low. We know why this occurs. Tb<sub>36</sub>Fe<sub>64</sub> is not the AOS compound, and only shows the pure thermal demagnetization. From the first seven pairs, we see that the experimental result for Tb<sub>30</sub>Fe<sub>70</sub> is reliable, since different pairs give a similar spin moment. But when it is paired with Tb<sub>36</sub>Fe<sub>64</sub>, it leads to an unreasonable result. This

means that the structure-property of Tb<sub>36</sub>Fe<sub>64</sub> is quite different from the AOS compounds such as Tb<sub>30</sub>Fe<sub>70</sub>, and it may not have the linear relation between the spin moment and the composition  $x$  as we assume above. Our finding is backed by the last pair, where Tb<sub>34</sub>Fe<sub>66</sub> is not an AOS compound initially, and only after the heating does it become AOS. If we look at Hassdenteufel's Fig. 7 [30], we find that Tb<sub>34</sub>Fe<sub>66</sub> does not follow the trend of the rest of the TbFe alloys. For this reason, they are not included in Table 1. Table 4 shows all the spin angular moments that are computed, with zero orbital angular momentum. Table 5 shows the same data but with bcc structure for Fe. The main conclusion is the same as Table 4.

**Helicity-dependent and helicity-independent all-optical spin switchings.** – There is enormous interest in both the all-optical helicity-dependent spin switching (AO-HDS) and the all-optical helicity-independent spin switching (AO-HIDS). Experimentally, Stanicu *et al.* [7] first demonstrated a clear helicity-dependent switching in GdFeCo, but when they [15] later increased the laser intensity, the switching became helicity-independent. In other words, there is a clear transition from a helicity-dependent switching to a helicity-independent switching in GdFeCo when one increases the laser fluence. The underlying reason of this transition has been unclear, though there are several mechanisms proposed [15]. On the other hand, Lambert *et al.* [18] demonstrated a clear helicity-dependent switching in their Co(0.4 nm)/Pt(0.7 nm)<sub>3</sub> film. At low laser power (362 nW), they showed that a reversed domain is written for  $\sigma^+$ , but not for  $\sigma^-$  or linearly polarized light. When they increased the laser power, regions of demagnetized random domains developed. Therefore, the helicity-independent switching does not occur in CoPt films. This may suggest that the difference between AO-HDS and AO-HIDS can both be laser-intensity dependent and material-dependent. Our model, which is solely based on a ferromagnet, does show a helicity-dependent switching. The light helicity is important for our model to work, as far as the laser fluence is small. For instance, if the spin points down (the  $-z$  axis), only the left-circularly polarized light can efficiently switch the spin up, if the laser field amplitude is weak. This finding appears to agree with the experimental results reasonably well [18]. If the laser field becomes too stronger, we are not completely confident whether our model can describe the physics correctly, though we did test the model in a single site case [24], where we found that the switching becomes highly nonlinear, and even the linearly polarized light can switch the spin. For this reason, our present paper exclusively focuses on the lower laser field limit and ferromagnets. We are currently exploring whether our model can describe GdFeCo. Our present model, without further change, is unsuitable for GdFeCo since GdFeCo is amorphous, ferrimagnetic and much more complicated. At minimum, we have to include the magnetic sublattices.



Table 1: Computed effective spin angular momentum for each element in GdFeCo and TbFe alloys. Multiple pairs of alloys are used to compute the effective spin angular momentum for several compounds to demonstrate the range of the change in the spin angular momentum. The sign convention of the spin angular momentum is that either Gd or Tb has a positive value, while Fe has a negative value. The original signs of those spin angular momentum are shown in Tables 2 through 5. A simple cubic structure is adopted for Fe.

Alloy	$S_{\text{Gd}}^{eff}(\hbar)$	$S_{\text{Fe}}^{eff}(\hbar)$	$S_{\text{Tb}}^{eff}(\hbar)$ (orbital free)	$S_{\text{Fe}}^{eff}(\hbar)$ (orbital free)
Gd <sub>28</sub> Fe <sub>63</sub> Co <sub>9</sub>	1.3414	-1.1691	—	—
Gd <sub>26</sub> Fe <sub>64.7</sub> Co <sub>9.3</sub>	1.2456	-1.2006	—	—
Gd <sub>25</sub> Fe <sub>65.6</sub> Co <sub>9.4</sub>	1.1517	-1.1777	—	—
Gd <sub>24</sub> Fe <sub>66.5</sub> Co <sub>9.5</sub>	1.2262	-1.3017	—	—
Gd <sub>24</sub> Fe <sub>66.5</sub> Co <sub>9.5</sub>	1.0867	-1.0113	—	—
Gd <sub>22</sub> Fe <sub>68.2</sub> Co <sub>9.8</sub>	1.1241	-1.3350	—	—
Gd <sub>22</sub> Fe <sub>68.2</sub> Co <sub>9.8</sub>	1.0135	-1.2244	—	—
Gd <sub>22</sub> Fe <sub>68.2</sub> Co <sub>9.8</sub>	0.9846	-0.7737	—	—
Gd <sub>22</sub> Fe <sub>74.6</sub> Co <sub>3.4</sub>	0.9846	-0.8463	—	—
Tb <sub>30</sub> Fe <sub>70</sub>	—	—	2.1506	-1.8385
Tb <sub>30</sub> Fe <sub>70</sub>	—	—	1.7594	-1.4473
Tb <sub>30</sub> Fe <sub>70</sub>	—	—	1.4952	-1.1831
Tb <sub>30</sub> Fe <sub>70</sub>	—	—	1.4698	-1.1577
Tb <sub>29</sub> Fe <sub>71</sub>	—	—	2.0789	-1.8648
Tb <sub>27</sub> Fe <sub>73</sub>	—	—	1.5835	-1.5093
Tb <sub>27</sub> Fe <sub>73</sub>	—	—	1.1867	-1.1125
Tb <sub>24</sub> Fe <sub>76</sub>	—	—	1.2641	-1.3452
Tb <sub>24</sub> Fe <sub>76</sub>	—	—	1.1758	-1.2569
Tb <sub>22</sub> Fe <sub>78</sub>	—	—	1.2789	-1.5007
Tb <sub>22</sub> Fe <sub>78</sub>	—	—	1.1587	-1.3806
Tb <sub>22</sub> Fe <sub>78</sub>	—	—	1.0965	-1.3183
Tb <sub>22</sub> Fe <sub>78</sub>	—	—	0.9669	-1.1887

Table 2: Computed effective spin angular momentum for each element in GdFeCo alloys for simple cubic Fe structure.

	$S_{\text{Gd}}^{\text{eff}}$	$S_{\text{Fe}}^{\text{eff}}$
Gd	$-10.2187\mu_B$	—
Fe	$3.9149\mu_B$	—
Gd24Fe66.5Co9.5	$-1.2262\hbar$	$1.3017\hbar$
Gd22Fe68.2Co9.8	$-1.1241\hbar$	$1.3350\hbar$
Gd	$9.5818\mu_B$	—
Fe	$-3.7114\mu_B$	—
Gd28Fe63Co9	$1.3414\hbar$	$-1.1691\hbar$
Gd26Fe64.7Co9.3	$1.2456\hbar$	$-1.2006\hbar$
Gd	$-9.2139\mu_B$	—
Fe	$3.5907\mu_B$	—
Gd25Fe65.6Co9.4	$-1.1517\hbar$	$1.1777\hbar$
Gd22Fe68.2Co9.8	$-1.0135\hbar$	$1.2244\hbar$
Gd	$-9.0562\mu_B$	—
Fe	$3.0415\mu_B$	—
Gd24Fe66.5Co9.5	$-1.0867\hbar$	$1.0113\hbar$
Gd22Fe74.6Co3.4	$-0.9962\hbar$	$1.1345\hbar$
Gd	$8.9509\mu_B$	—
Fe	$-2.2689\mu_B$	—
Gd22Fe68.2Co9.8	$0.9846\hbar$	$-0.7737\hbar$
Gd22Fe74.6Co3.4	$0.9846\hbar$	$-0.8463\hbar$

Table 3: Computed effective spin angular momentum for each element in GdFeCo alloys for bcc Fe structure.

	$S_{\text{Gd}}^{\text{eff}}$	$S_{\text{Fe}}^{\text{eff}}$
Gd	$-7.4560\mu_B$	—
Fe	$2.8615\mu_B$	—
Gd24Fe66.5Co9.5	$-0.8947\hbar$	$0.9514\hbar$
Gd22Fe68.2Co9.8	$-0.8202\hbar$	$0.9758\hbar$
Gd	$7.4926\mu_B$	—
Fe	$-2.9045\mu_B$	—
Gd28Fe63Co9	$1.0490\hbar$	$-0.9149\hbar$
Gd26Fe64.7Co9.3	$0.9740\hbar$	$-0.9396\hbar$
Gd	$-6.7695\mu_B$	—
Fe	$2.6400\mu_B$	—
Gd25Fe65.6Co9.4	$-0.8462\hbar$	$0.8659\hbar$
Gd22Fe68.2Co9.8	$-0.7446\hbar$	$0.9002\hbar$
Gd	$-6.6669\mu_B$	—
Fe	$2.2355\mu_B$	—
Gd24Fe66.5Co9.5	$-0.8000\hbar$	$0.7433\hbar$
Gd22Fe74.6Co3.4	$-0.7334\hbar$	$0.8339\hbar$
Gd	$6.7532\mu_B$	—
Fe	$-1.7221\mu_B$	—
Gd22Fe68.2Co9.8	$0.7428\hbar$	$-0.5873\hbar$
Gd22Fe74.6Co3.4	$0.7428\hbar$	$-0.6424\hbar$

Table 4: Computed effective spin angular momentum for each element in TbFe alloys for simple cubic Fe structure.

	$S_{\text{Tb}}^{\text{eff}}$	$S_{\text{Fe}}^{\text{eff}}$
Tb	$14.3375\mu_B$	—
Fe	$-5.2529\mu_B$	—
Tb30Fe70	$2.1506\hbar$	$-1.8385\hbar$
Tb29Fe71	$2.0789\hbar$	$-1.8648\hbar$
Tb	$11.7296\mu_B$	—
Fe	$-4.1352\mu_B$	—
Tb30Fe70	$1.7594\hbar$	$-1.4473\hbar$
Tb27Fe73	$1.5835\hbar$	$-1.5093\hbar$
Tb	$-11.6262\mu_B$	—
Fe	$3.8479\mu_B$	—
Tb22Fe78	$-1.2789\hbar$	$1.5007\hbar$
Tb19Fe81	$-1.1045\hbar$	$1.5584\hbar$
Tb	$-10.5340\mu_B$	—
Fe	$3.5399\mu_B$	—
Tb22Fe78	$-1.1587\hbar$	$1.3806\hbar$
Tb24Fe76	$-1.2641\hbar$	$1.3452\hbar$
Tb	$9.9679\mu_B$	—
Fe	$-3.3802\mu_B$	—
Tb22Fe78	$1.0965\hbar$	$-1.3183\hbar$
Tb30Fe70	$1.4952\hbar$	$-1.1831\hbar$
Tb	$9.7986\mu_B$	—
Fe	$-3.3076\mu_B$	—
Tb30Fe70	$1.4698\hbar$	$-1.1577\hbar$
Tb24Fe76	$1.1758\hbar$	$-1.2569\hbar$
Tb	$-8.7901\mu_B$	—
Fe	$3.0480\mu_B$	—
Tb22Fe78	$-0.9669\hbar$	$1.1887\hbar$
Tb27Fe73	$-1.1867\hbar$	$1.1125\hbar$
Tb	$5.3268\mu_B$	—
Fe	$-1.3912\mu_B$	—
Tb36Fe64	$0.9588\hbar$	$-0.4452\hbar$
Tb30Fe70	$0.7990\hbar$	$-0.4869\hbar$
Tb	$2.1818\mu_B$	—
Fe	$-0.4756\mu_B$	—
Tb34Fe66	$0.3709\hbar$	$-0.1570\hbar$
Tb24Fe76	$0.2618\hbar$	$-0.1807\hbar$

Table 5: Computed effective spin angular momentum for each element in TbFe alloys for bcc Fe structure.

		$S_{\text{Tb}}^{\text{eff}}$	$S_{\text{Fe}}^{\text{eff}}$
Tb	$11.2034\mu_B$	—	
Fe	$-4.1158\mu_B$	—	
Tb30Fe70		$1.6805\hbar$	$-1.4405\hbar$
Tb29Fe71		$1.6245\hbar$	$-1.4611\hbar$
Tb	$9.0822\mu_B$	—	
Fe	$-3.2067\mu_B$	—	
Tb30Fe70		$1.3623\hbar$	$-1.1224\hbar$
Tb27Fe73		$1.2261\hbar$	$-1.1705\hbar$
Tb	$-7.8075\mu_B$	—	
Fe	$2.6098\mu_B$	—	
Tb22Fe78		$-0.8588\hbar$	$1.0178\hbar$
Tb19Fe81		$-0.7417\hbar$	$1.0570\hbar$
Tb	$-7.4627\mu_B$	—	
Fe	$2.5126\mu_B$	—	
Tb22Fe78		$-0.8209\hbar$	$0.9799\hbar$
Tb24Fe76		$-0.8955\hbar$	$0.9548\hbar$
Tb	$7.4621\mu_B$	—	
Fe	$-2.5124\mu_B$	—	
Tb22Fe78		$0.8208\hbar$	$-0.9798\hbar$
Tb30Fe70		$1.1193\hbar$	$-0.8793\hbar$
Tb	$7.4619\mu_B$	—	
Fe	$-2.5123\mu_B$	—	
Tb30Fe70		$1.1193\hbar$	$-0.8793\hbar$
Tb24Fe76		$0.8954\hbar$	$-0.9547\hbar$
Tb	$-6.3789\mu_B$	—	
Fe	$2.2069\mu_B$	—	
Tb22Fe78		$-0.7017\hbar$	$0.8607\hbar$
Tb27Fe73		$-0.8611\hbar$	$0.8055\hbar$
Tb	$4.4942\mu_B$	—	
Fe	$-1.2404\mu_B$	—	
Tb36Fe64		$0.8090\hbar$	$-0.3969\hbar$
Tb30Fe70		$0.6741\hbar$	$-0.4342\hbar$
Tb	$1.7919\mu_B$	—	
Fe	$-0.4100\mu_B$	—	
Tb34Fe66		$0.3046\hbar$	$-0.1353\hbar$
Tb24Fe76		$0.2150\hbar$	$-0.1558\hbar$

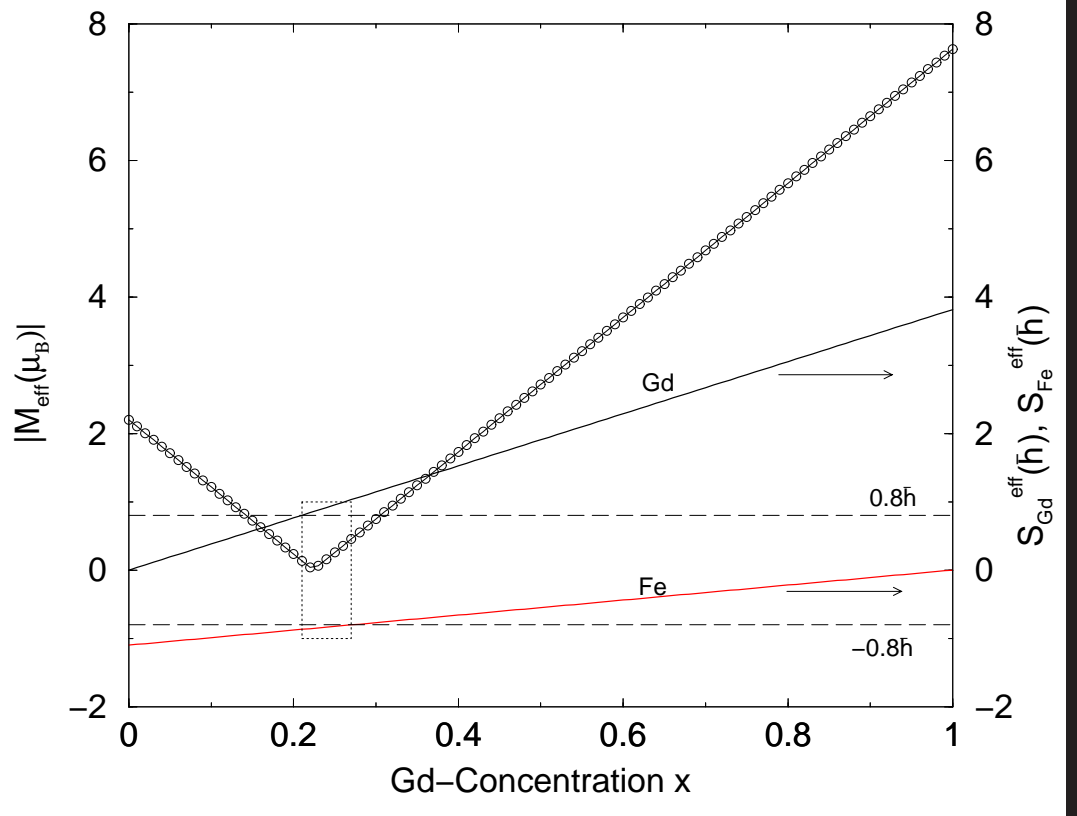


Fig. 6: Effective spin moment change as a function of Gd concentration  $x$  (circles). The two solid lines represent the effective spin angular momentum for Gd and Fe (using the right axis). The two horizontal dashed lines denote the predicted critical spin angular momentum ( $\pm 0.8\hbar$ ). The dotted line box highlights the narrow region of the Gd concentration where spin angular momentum satisfies our criterion and the spin reversal occurs.